10

Large-Signal Modeling of GaN Devices for Designing High Power Amplifiers of Next Generation Wireless Communication Systems

Anwar Jarndal
Hodeidah University
Yemen

1. Introduction

An excellent candidate for fabrication of high-power amplifiers (HPAs) for next-generation wireless communication systems is a GaN HEMT. It has high sheet carrier density and high saturation electron velocity, which produce high output power. It also has high electron mobility, which is largely responsible for low on-resistance value which enhances high-power-added efficiency. As a result of GaN as a wideband material, the GaN HEMTs can achieve very high breakdown voltage and very high current density, and they can sustain very high channel-operating temperature. Furthermore, a possible epitaxial growth on silicon carbide substrate, which has excellent thermal properties, makes this device optimal for high-power RF applications. The past decade saw rapid progress in the development of GaN HEMTs with a focus on its power performance (Eastman et al., 2001). However, despite the high output power of this device, current dispersion is the biggest obstacle in obtaining reproducible power performance (Vetury et al., 2001); (Meneghesso et al., 2004). Designing an HPA based on the GaN HEMTs requires an accurate large-signal model for this device. This model should account for the current dispersion and temperature-dependent performance in addition to other high-power-stimulated effects like gate forward and breakdown phenomenon. In particular, the model should be able to predict intermodulation distortion (IMD), which is very important for the analysis of the HPA nonlinearity. In the last decade different models have been developed for GaN HEMTs. The analytical models reported in (Green et al., 2000) and (Lee & Webb, 2004) can simulate the fundamental output power including the current dispersion and thermal characteristics of the GaN HEMTs. However, these models have poor IMD-prediction capabilities. In another reported model (Raay et al., 2003), no IMD simulation has been presented. The model published in (Cabral et al., 2004) has been optimized for IMD simulation, but it does not account for the current dispersion or the temperature-dependent characteristics. This chapter addresses the development of a large-signal model for GaN HEMTs, which can simulate all of the mentioned effects in an efficient manner. First, a small-signal model that will be used as a basis for constructing the large-signal model will be described. Detailed steps for extraction of the small-signal model parameters will be presented. Large-signal

modeling and extraction procedures will also be explained. Finally, the developed large-signal model will be validated by comparing its simulations with measurements.

2. GaN HEMT

The general structure of the investigated devices is shown in Figure 1. The GaN HEMT structure was grown on SiC 2-inch wafers using Metal-Organic-Chemical-Vapour-Deposition (MOCVD) technology (Lossy[a] et al., 2002). This substrate provides an excellent thermal conductivity of 3.5 W/cm, which is an order of magnitude higher than that of sapphire. The epitaxial growth structure starts with the deposition of a 500 nm thick graded AlGaN layer on the substrate to reduce the number of threading dislocations in the GaN buffer layer due to the lattice mismatch between GaN and SiC layers. These threading dislocations enhance buffer traps and hence the associated drain-current dispersion (Hansen et al., 1998). A 2.7 µm thick highly insulating GaN buffer layer is then deposited to get lower background carrier concentration, which accordingly results in increased electron mobility in the above unintentionally doped layers. The buffer layer is followed by a 3 nm $Al_{0.25}Ga_{0.75}N$ spacer, 12 nm Si-doped $Al_{0.25}Ga_{0.75}N$ supply layer (5x1018 cm^{-3}), and 10 nm $Al_{0.25}Ga_{0.75}N$ barrier layer. The spontaneous and piezoelectric polarizations of the $Al_{0.25}Ga_{0.75}N$ layers form a two-dimensional electron gas (2DEG) at the AlGaN/GaN interface (Ambacher et al., 1999). The spacer layer is included to reduce the ionized-impurity scattering that deteriorates electron mobility in the 2DEG. The whole structure is capped with a 5 nm thick GaN layer to increase the effective Schottky barrier, which improves the breakdown characteristics and decreases the gate leakage. The measured 2DEG electron density and mobility, at room temperature, are 7.8×10^{12} cm^{-2} and 1400 cm^2/Vs (Lossy[a] et al., 2002). Device fabrication is accomplished using 0.5-µm stepper lithography, which results in an excellent homogeneity of the electrical properties over the wafer (Lossy et al., 2001).

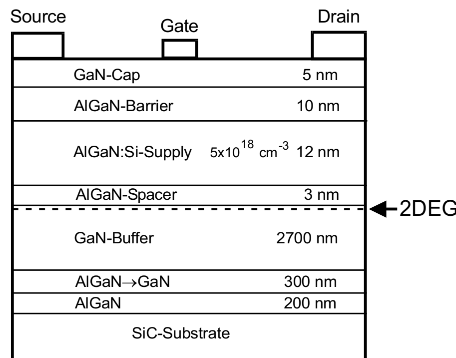

Fig. 1. Epitaxial layer structure of GaN HEMT.

Source and drain ohmic contacts have a metallization consisting of Ti/Al/Ti/Au/WSiN (10/50/25/30/120 nm) with improved edge and surface morphology. Due to the properties of the WSiN sputter deposition process, the Ti/Al/Ti/Au layers, which are deposited by e-beam evaporation, are totally embedded. The source and drain contacts are then rapidly thermal-annealed at 850 °C. The contact resistance is analyzed by Thermal Lens Microscope

(TLM) measurements with respect to thickness and composition of the different metallization layers at different temperatures. The contact resistance is determined to be 0.25-0.5 Ωmm under these conditions (Lossy[a] et al., 2002). Gate contacts are made from a Pt/Au metallization, and a gate length of 0.5μm is obtained using stepper lithography. Additionally, devices with gate length less than 0.3μm are written using a shaped electron beam tool (ZBA23-40kV) (Lossy[b] et al., 2002). SiN passivation layer is then deposited to reduce the surface trapping induced drain-current dispersion. Field plate connected to the gate, at the gate pad, and deposited over the passivation layer was employed for some investigated devices to improve its breakdown characteristics. An air-bridge technology using an electroplated Au is used to connect the source pads of multifinger devices.

3. Small-signal modeling

In bottom-up modeling technique, a multibias small-signal measurement is carried out over a range of bias points, and a large-signal model is then determined from the small-signal model derived at each of these bias points. Therefore, the accuracy of the constructed large-signal model depends on the accuracy of the bias-dependent small-signal model, which should reflect the electrical and physical characteristics of the device. Accurate determination of the intrinsic bias-dependent circuit of GaN HEMT small-signal model requires an efficient extraction method for the parasitic elements of the device. In (Jarndal & Kompa, 2005), an efficient reliable model parameter extraction method, applied for GaN HEMT, was developed. This method uses only a cold S-parameter measurement for accurate determination of the parasitic elements. The main advantage of this method is that it gives reliable values for the parasitic elements of the device without need for additional measurements or separate test patterns. Since the knowledge of distributed effects is important to identify the device parasitic elements for further minimization, a 22-element distributed model shown in Figure 2 is used as a small-signal model for GaN HEMT. This model is general and applicable for large gate periphery devices. The main advantages of this model are as follows.

- It accounts for all expected parasitic elements of the device.
- It reflects the physics of the device over a wide bias and frequency range.

Therefore, this model can be suitable for scalable large-signal model construction.

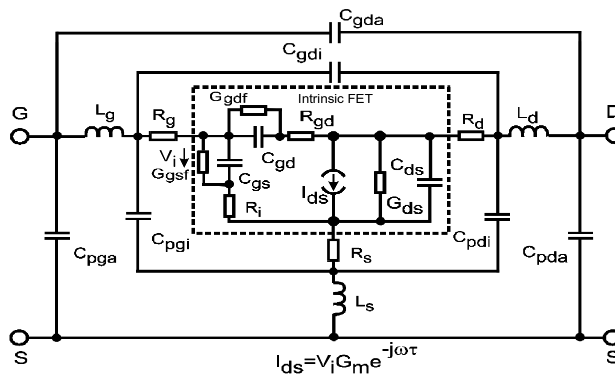

Fig. 2. 22-element distributed small-signal model for active GaN HEMT.

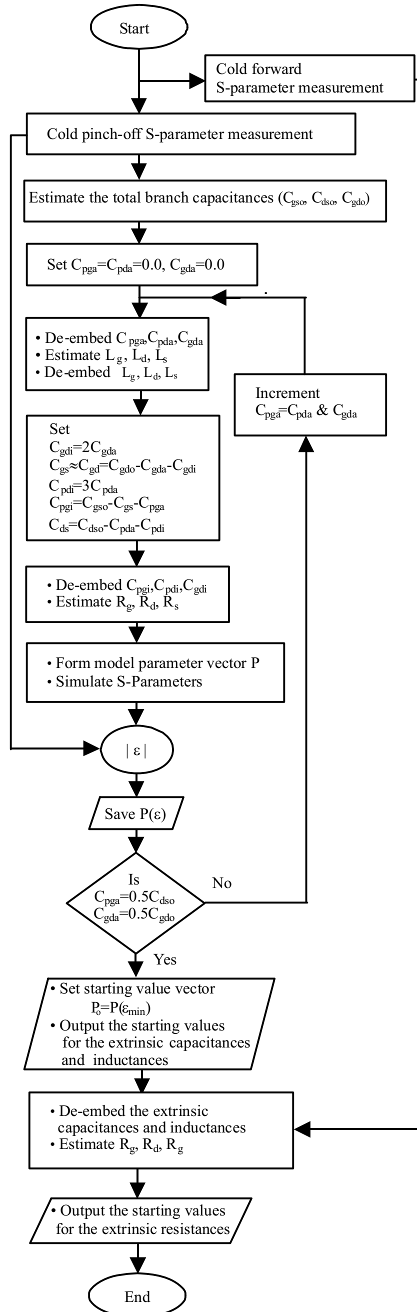

Fig. 3. Flowchart of the small-signal model parameter starting value generation algorithm. © 2005 IEEE. Reprinted with permission.

In the extrinsic part of this model, C_{pga}, C_{pda} and C_{gda} account for parasitic elements due to the pad connections, measurement equipment, probes, and probe tip-to-device contact transitions; while C_{pgi}, C_{pdi}, and C_{gdi} account for interelectrode and crossover capacitances (due to air–bridge source connections) between gate, source, and drain. R_g, R_d, and R_s represent contact and semiconductor bulk resistances; while L_g, L_d, and L_s model effect of metallization inductances. In the intrinsic part, charging and discharging process for depletion region under the gate is described by C_{gs}, R_i, C_{gd} and R_{gd}. The gate forward and breakdown conductions are represented by G_{gsf} and G_{gdf}, respectively. Variation of the channel conduction with remote gate voltage is described by G_m; while the channel conductance controlled by local drain voltage is represented by G_{ds}. C_{ds} model the capacitance between the drain and source electrodes separated by the depletion region in electrostatic sense. Transit time of electrons in the channel at high-speed input signal is described by τ.

3.1 Extrinsic parameter extraction

Many of the model parameters in Figure 2 are difficult if not impossible to determine directly from measurements. Therefore, these parameters are determined through an optimization algorithm. The efficiency of this algorithm depends on the quality of starting values and the number of optimization variables. Under cold pinch-off condition, the equivalent circuit in Figure 2 can be simplified by excluding some elements, thereby reducing the number of unknowns. For further minimization of the number of optimization variables, only the extrinsic elements of the model will be optimized, while the intrinsic elements are determined from the deembedded Y-parameters. Under this bias condition, the reactive elements of the model are strongly correlated (Jarndal & Kompa, 2005). Therefore, the starting values estimation can be carried out in a way that takes this correlation into account. In addition, the S-parameter measurements must cover the frequency range where this correlation is more obvious. The required measurements frequency range for reliable starting values generation reduces for larger devices, e.g., up to 20 GHz for an 8x125-µm device. The proposed technique for starting values generation is based on searching for the optimal distribution of the total capacitances. This is achieved by scanning the outer capacitance values within the specified ranges. For each scanned value, the interelectrode capacitances are assigned suitable values and then deembedded from the measured Y-parameters. The rest of the model parameters are then estimated from the stripped Y-parameters. The whole estimated parameters are then used to simulate the device S-parameters, which are then compared with the measured ones. Using this systematic searching procedure, high-quality measurement-correlated starting values for the small-signal model parameters can be found. The closeness of the starting values to the real values simplifies the next step of parameters optimization since the risk of a local minimum is minimized.

A. Generation of starting value of small-signal model parameters

The starting values generation procedure is described by the flowchart in Figure 3. As shown in this flowchart, the starting values of the extrinsic capacitances and inductances are generated from pinch-off measurements, while those of extrinsic resistances are generated

from forward measurements. The whole starting values generating procedure can be summarized as follows.

Step 1) Let $V_{GS} < -V_{pinch\text{-}off}$ and $V_{DS} = 0.0$ V. In this case, the equivalent circuit in Figure 2 of the active device can be used for this cold pinch-off device if the drain current source and the output channel conductance are excluded. Moreover, at low frequencies (in the megahertz range), this circuit can be reduced to a capacitive network shown in Figure 4 and the Y-parameters of this equivalent circuit can be written as

$$Y_{11} = j\omega\,(C_{gso} + C_{gdo}) \tag{1}$$

$$Y_{22} = j\omega\,(C_{dso} + C_{gdo}) \tag{2}$$

$$Y_{12} = Y_{21} = -j\omega\, C_{gdo} \tag{3}$$

where

$$C_{gdo} = C_{gda} + C_{gdi} + C_{gd} \tag{4}$$

$$C_{gso} = C_{pga} + C_{pgi} + C_{gs} \tag{5}$$

$$C_{dso} = C_{pda} + C_{pdi} + C_{ds}\,. \tag{6}$$

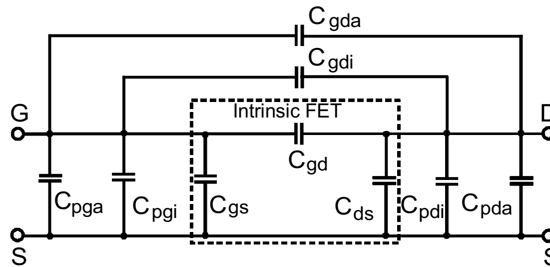

Fig. 4. Equivalent circuit model for cold pinch-off GaN HEMT at low frequency.

The total capacitances for gate–source, gate–drain, and drain–source branches are determined from the low frequency range of pinch-off S-parameter measurements, which are converted to Y-parameter.

Step 2) The next step is searching for the optimal distribution of the total capacitances, which gives the minimum error between the measured and simulated S-parameters. This is achieved by scanning C_{pga}, C_{pda} , and C_{gda} values within the specified ranges. C_{pga} and C_{pda} are scanned from 0 to $0.5C_{dso}$ while C_{gda} is scanned from 0 to $0.5C_{gdo}$. During the scanning process, C_{pga} is assumed to be equal to C_{pda}

$$C_{pga} \cong C_{pda}\,. \tag{7}$$

The gate–drain interelectrode capacitance C_{gdi} is assumed to be twice the C_{gda} pad capacitance value

$$C_{gdi} \cong 2C_{gda}\,. \tag{8}$$

For symmetrical gate–source and gate–drain spacing, the depletion region will be uniform under pinch-off, so that

$$C_{gs} \cong C_{gd} = C_{gdo} - C_{gdi} - C_{gda}. \tag{9}$$

The value of C_{pgi} is calculated using

$$C_{pgi} = C_{gso} - C_{gs} - C_{pga}. \tag{10}$$

With the GaN devices under analysis, C_{pdi} is a significant part of the total drain–source capacitance. Therefore, it is found that the assumption

$$C_{pdi} \cong 3\,C_{pda} \tag{11}$$

minimizes the error between the simulated and measured S-parameters. For medium and high frequency range, the intrinsic transistor of the pinch-off model is represented in T-network as shown in Figure 5 where the interelectrode capacitances (C_{pgi}, C_{pdi} , and C_{gdi}) have been absorbed in the intrinsic capacitances (C_{gs} , C_{ds} , and C_{gd}). The values for C_{pga}, C_{pda} , and C_{gda} are deembedded from Y-parameter and then converted to Z-parameter.

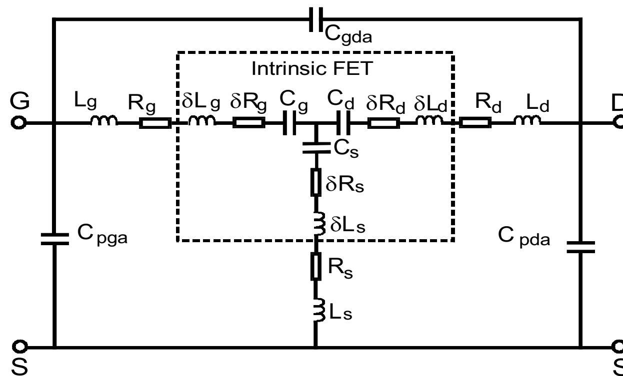

Fig. 5. Equivalent circuit model for cold pinch-off GaN HEMT at medium and high frequency.

This stripped Z-parameter can be written as

$$Z_{11} = R_g + R_s + j\omega(L_g + L_s) + \frac{1}{j\omega}\left(\frac{1}{C_g} + \frac{1}{C_s}\right) + \delta Z_g \tag{12}$$

$$Z_{22} = R_d + R_s + j\omega(L_d + L_s) + \frac{1}{j\omega}\left(\frac{1}{C_d} + \frac{1}{C_s}\right) + \delta Z_d \tag{13}$$

$$Z_{12} = Z_{21} = R_s + j\omega L_s + \frac{1}{j\omega C_s} + \delta Z_s \tag{14}$$

where

$$\delta Z_g = \delta R_g + \delta R_s + j\omega(\delta L_g + \delta L_s) \tag{15}$$

$$\delta Z_d = \delta R_d + \delta R_s + j\omega(\delta L_d + \delta L_s) \tag{16}$$

$$\delta Z_s = \delta R_s + j\omega\delta L_s \,. \tag{17}$$

δZ_g, δZ_d, and δZ_s represent correction terms related to the intrinsic parameters of the model. Ignoring the correction terms and multiplying the Z-parameters by ω and then taking the imaginary parts gives

$$\mathrm{Im}[\omega Z_{11}] = (L_g + L_s)\omega^2 - \left(\frac{1}{C_g} + \frac{1}{C_s}\right) \tag{18}$$

$$\mathrm{Im}[\omega Z_{22}] = (L_d + L_s)\omega^2 - \left(\frac{1}{C_d} + \frac{1}{C_s}\right) \tag{19}$$

$$\mathrm{Im}[\omega Z_{12}] = L_s\omega^2 - \frac{1}{C_s} \,. \tag{20}$$

Hence, the values of L_g, L_d , and L_s can be extracted from the slope of $\mathrm{Im}[\omega Z_{ij}]$ versus ω^2 curve. The estimated values of the inductances described above and the interelectrode capacitances (C_{pgi}, C_{pdi}, and C_{gdi}) are deembedded. However, the incomplete deembedding of the outer capacitances and the inductances introduce nonlinear frequency dependence in the real part of deembedded Z-parameters. By multiplying the deembedded Z-parameter by ω^2, this effect is reduced (Jarndal & Kompa, 2005). Ignoring the correction terms and multiplying the deembedded Z-parameter by ω^2 and then taking the real part of this Z–parameter gives

$$\mathrm{Re}\left[\omega^2 Z_{11}\right] = \omega^2 \left(R_g + R_s\right) \tag{21}$$

$$\mathrm{Re}\left[\omega^2 Z_{22}\right] = \omega^2 \left(R_d + R_s\right) \tag{22}$$

$$\mathrm{Re}\left[\omega^2 Z_{12}\right] = \omega^2 R_s \,. \tag{23}$$

By linear regression, the value of R_g+R_s, R_d+R_s, and R_s can be extracted from the slope of $\mathrm{Re}[\omega^2 Z_{ij}]$ versus ω^2 curves. The resulting estimated parameters are used to simulate the device S-parameters, which are then compared with the measured ones to calculate the residual fitting error (ε). The outer capacitances (C_{pga}, C_{pda}, and C_{gda}) are incremented, and the procedure is repeated until C_{pga} (C_{pda}) is equal to $0.5C_{dso}$ and C_{gda} is equal to $0.5C_{gdo}$. The vector of model parameters $P(\varepsilon_{min})$, corresponding to the lowest error ε_{min}, is then taken as the appropriate starting value.

Step 3) Because of unavoidable high measurement uncertainty for cold pinch-off device, the determination of a reliable starting value for the extrinsic resistances is difficult if not impossible. More reliable starting value was generated using cold gate forward S-parameter measurements at high gate voltage greater than or equal to 2 V. This is due to the higher conduction band of GaN-based HEMT with respect to the corresponding GaAs-based HEMT. Therefore, significantly higher voltages have to be applied to reach the condition when the influence of the gate capacitance is negligible. The determined values of extrinsic capacitances and inductances, in Step 2), are deembedded from the gate-forward measurements. The starting values of the extrinsic resistances are then estimated from the stripped forward Z–parameters.

B. Model parameter optimization

The procedure for the generation of starting values of the model parameters was discussed in Section 3.1-A. Here, the result of the optimal value for each model parameter is presented. Model parameters optimization has been done based on the principle of bidirectional optimization technique proposed by Lin and Kompa (Lin & Kompa, 1994). This technique works successfully for lumped small-signal model, but cannot be used efficiently for distributed model. This is due to the extra parasitic elements of this model, which increase the searching space. Now, this algorithm can be modified to become applicable for the distributed model, where the closeness of the generated starting value to the true value allows the searching space to be reduced by optimizing only the extrinsic parameters. At each iteration through the optimization process, the extrinsic parameters are assigned suitable values and then deembedded from the measured data to determine the intrinsic Y-parameters. The intrinsic model parameters are then estimated by means of data fitting from the deembedded measurements. The whole estimated model parameters are then used to fit the measured S-parameters. This process is continued to find the optimal model parameters. In this case, the optimization problem is a nonlinear multidimensional one, whose objective function is likely to have multiple local minima. Furthermore, the cold pinch-off device measurements have a high uncertainty (HP8510B network analyzer manual, 1987). These two factors increase the probability of trapping into a local minimum, which requires a careful formulation for the objective function to avoid the local minimum problem. The magnitude of the error between the measured S-parameter and its simulated value can be expressed as (Jarndal & Kompa, 2005)

$$\varepsilon_{ij} = \frac{\left|\mathrm{Re}(\delta S_{ij,n})\right| + \left|\mathrm{Im}(\delta S_{ij,n})\right|}{W_{ij}} \quad , \mathrm{i,j} = 1,2;\ \mathrm{n} = 1,2,\ldots,\mathrm{N} \tag{24}$$

where

$$W_{ij} = \max[\left|S_{ij}\right|] \quad , \mathrm{i,j} = 1,2;\ \mathrm{i} \neq \mathrm{j} \tag{25}$$

$$W_{ii} = 1 + \left|S_{ii}\right| \quad , \mathrm{i} = 1,2 \tag{26}$$

and N is the total number of data points. δS is the difference between the measured S-parameter coefficient and its simulated value. The weighting factor (W) deemphasizes data region with higher reflection coefficients due to the involved higher measurement uncertainty. The scalar error is then expressed as

$$\varepsilon_s = \frac{1}{N} \sum_{n=1}^{N} \left\| \overset{*}{\varepsilon}(f_n) \right\|_1 \tag{27}$$

where

$$\overset{*}{\varepsilon}(f_n) = \begin{bmatrix} \varepsilon_{11}(f_n) & \varepsilon_{12}(f_n) \\ \varepsilon_{21}(f_n) & \varepsilon_{22}(f_n) \end{bmatrix} \tag{28}$$

defined at each frequency point. However, the objective function that is based on S-parameters alone to minimize the fitting error may not necessarily lead to physically relevant values of the model parameters (Kompa & Novotny, 1997). For further

enhancement of the objective function, another performance quantity, depending on the final application, will be considered. The main application of GaN-based HEMT is power amplifier design. For power amplifier design, the output and input impedance, the device gain, and stability factor are important for the design of matching networks. These factors can be expressed as a function of S–parameters and fitted during the optimization. The stability factor defined at the output plane of the device at each frequency can be expressed as

$$K = \frac{1 - |S_{22}|^2}{\left|S_{22} - S_{11}^* \Delta_s\right| + |S_{12} S_{21}|} \tag{29}$$

where S^* is the complex conjugate and Δ_s is the determinant of S-parameter matrix at each frequency (Edwards & Sinsky, 1992). The fitting error of the stability factor is given by

$$\varepsilon_K = \frac{1}{N} \sum_{k=1}^{N} |K_{meas} - K_{sim}| \tag{30}$$

where K_{meas} and K_{sim} are the stability factors from the measured and simulated S-parameters, respectively. With regard to the device gain, the maximally efficient gain defined in (Kotzebue,1976) is a more suitable one, since it remains finite even for an unstable device. This gain may be defined at each frequency as

$$G = \frac{|S_{21}|^2 - 1}{\ln |S_{21}|^2} . \tag{31}$$

The error in the gain may thus, be expressed as

$$\varepsilon_G = \frac{1}{N} \sum_{m=1}^{N} |G_{meas} - G_{sim}| \tag{32}$$

where G_{meas} and G_{sim} are the gains computed from the measured and modeled S-parameters. The fitting error can be defined in terms of the three error components as

$$\varepsilon = \sqrt{\frac{1}{3}\left(\varepsilon_s{}^2 + \varepsilon_K{}^2 + \varepsilon_G{}^2\right)} . \tag{33}$$

The modified Simplex optimization algorithm proposed in (Kompa & Novotny, 1997) is used to minimize the objective function in (33).

The extraction procedure was applied to different GaN HEMT sizes. Table 1 presents the final optimised results for extrinsic parameters extraction. As it can be observed in the table, the extracted pad capacitances (C_{pga}, C_{pda} , and C_{gda}) are in proportion with the gate width. There is no significant difference between the pad capacitances of 8x125-µm and 8x250-µm devices because the pad connection area is related mainly to the number of fingers. The inter-electrode capacitances (C_{pdi} and C_{gdi}) are also in proportion with the gate width. Due to the small values of R_g and R_s, for larger devices, C_{pgi} cannot be separated completely from the intrinsic capacitance C_{gs}. However, the sum of C_{pgi} and C_{gs} is in proportion with the gate width. By direct scaling of the 8x250-µm device, the expected values of C_{gda} and C_{gdi} for

8x125-µm device are 20 fF and 40 fF, respectively. Due to the smaller values of these elements and also due to the smaller values of L_g and L_d for this device, C_{gda} and C_{gdi} cannot be separated form C_{gd}. The parasitic inductance includes the self-inductance due the metallization contact and the mutual inductance between the metal interconnection. The mutual inductance increases by increasing the number of fingers. For this reason, there is a considerable increase of L_d and L_g values for 16x250-µm device with respect to 8x125-µm device (Jarndal[a] & Kompa, 2006). The parasitic resistances (R_d and R_s) are inversely proportional with the gate width. However, this is not the case with R_g, which is proportional with the unite-gate-width and inversely proportional with the number of gate fingers as reported in (Goyal et al., 1989).

Parameter	W_g = 16x250 µm	W_g = 8x250 µm	W_g = 8x125 µm	W_g = 2x50 µm
C_{pga} (fF)	233.5	89.8	86.9	9.97
C_{pgi} (fF)	39.6	234.8	332.2	7.09
C_{gs} (fF)	1508.4	538.6	255.8	15.38
C_{gda} (fF)	121.6	41.7	0.0	0.47
C_{gdi} (fF)	265.6	96.5	0.0	0.86
C_{gd} (fF)	1285.7	757.8	517.4	20.17
C_{pda} (fF)	206.4	90.9	86.3	7.13
C_{pdi} (fF)	790.7	390.2	245	29.42
C_{ds} (fF)	0.0	0.0	1.0	0.0
L_g (pH)	122.3	81.9	57.3	46.55
L_d (pH)	110.9	75.4	54.5	47.9
L_s (pH)	3.6	5.7	5.6	6.25
R_g (Ω)	1.1241	2.8	1.7	4.8
R_d (Ω)	0.71424	1.4	2.3	11.8
R_s (Ω)	0.25152	0.5	0.9	5.47
R_i (Ω)	0.0	0.0	0.0	0.0
R_{gd} (Ω)	0.1	0.0	0.0	0.0
G_m (mS)	0.0	0.0	0.0	0.0
τ (ps)	0.0	3.3	0.0	0.0
G_{ds} (mS)	0.34	0.0	0.26	0.0
G_{gsf} (mS)	2.3	0.6	0.4	0.0
G_{gdf} (mS)	0.24	0.25	0.2	0.0

Table 1. Extracted model parameters for different GaN HEMT sizes under cold pinch-off bias condition (V_{DS} = 0 V and $V_{GS} = V_{pinch\text{-}off}$). © 2006 IEEE. Reprinted with permission.

3.2 Intrinsic parameter extraction

After deembedding the extracted extrinsic parameters in Section 3.1, the bias-dependent intrinsic parameters can be extracted. An efficient technique is developed for extracting of the optimal value of the intrinsic element. In this technique, the intrinsic Y–parameters are formulated in a way where the optimal intrinsic element value can be extracted using simple linear data fitting (Jarndal & Kompa, 2005). The admittance for the intrinsic gate–source branch Y_{gs} is given by

$$Y_{gs} = Y_{i,11} + Y_{i,12} = \frac{G_{gsf} + j\omega C_{gs}}{1 + R_i G_{gsf} + j\omega R_i C_{gs}} . \quad (34)$$

By defining a new variable D as

$$D = \frac{|Y_{gs}|^2}{\mathrm{Im}[Y_{gs}]} = \frac{G_{gsf}^{\ 2}}{\omega C_{gs}} + \omega C_{gs} . \quad (35)$$

C_{gs} can be determined from the slope of the curve for ωD versus ω^2 by linear fitting, where ω is the angular frequency. By redefining D as

$$D = \frac{Y_{gs}}{\mathrm{Im}[Y_{gs}]} = \frac{G_{gsf}(1 + R_i G_{gsf})}{\omega C_{gs}} + \omega R_i C_{gs} - j . \quad (36)$$

R_i can be determined from the plot of the real part of ωD versus ω^2 by linear fitting. G_{gsf} can be determined from the real part of Y_{gs} at low frequencies (in the megahertz range). The admittance for the intrinsic gate–drain branch Y_{gd} is given by

$$Y_{gd} = -Y_{i,12} = \frac{G_{gdf} + j\omega C_{gd}}{1 + R_{gd} G_{gdf} + j\omega R_{gd} C_{gd}} . \quad (37)$$

The same procedure, given in (35) and (36), can be used for extracting C_{gd}, R_{gd}, and G_{gdf}. The admittance of the intrinsic transconductance branch Y_{gm} can be expressed as

$$Y_{gm} = Y_{i,21} - Y_{i,12} = \frac{G_m e^{-j\omega\tau}}{1 + R_i G_{gsf} + j\omega C_{gs}} . \quad (38)$$

By redefining D as

$$D = \left| \frac{Y_{gs}}{Y_{gm}} \right|^2 = \left(\frac{G_{gsf}}{G_m} \right)^2 + \left(\frac{C_{gs}}{G_m} \right)^2 \omega^2 . \quad (39)$$

G_m can be determined from the slope of the curve for D versus ω^2 by linear fitting. By redefining D as

$$D = (G_{gsf} + j\omega C_{gs}) \frac{Y_{gm}}{Y_{gs}} = G_m e^{-j\omega\tau} . \quad (40)$$

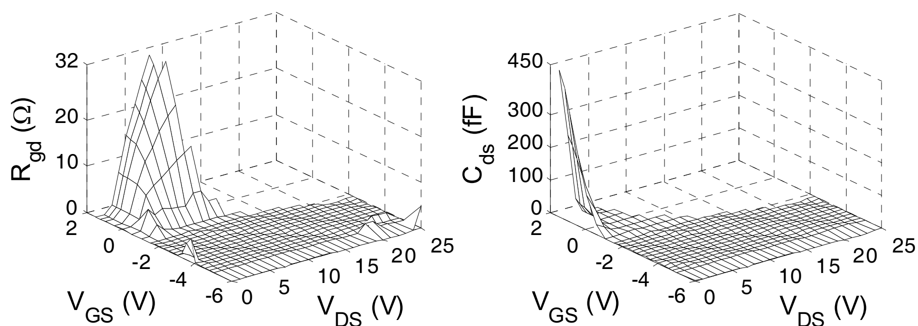

Fig. 6. Extracted R_{gd} and C_{ds} as a function of the extrinsic voltages for a GaN HEMT with a 2x50-μm gate width. © 2005 IEEE. Reprinted with permission.

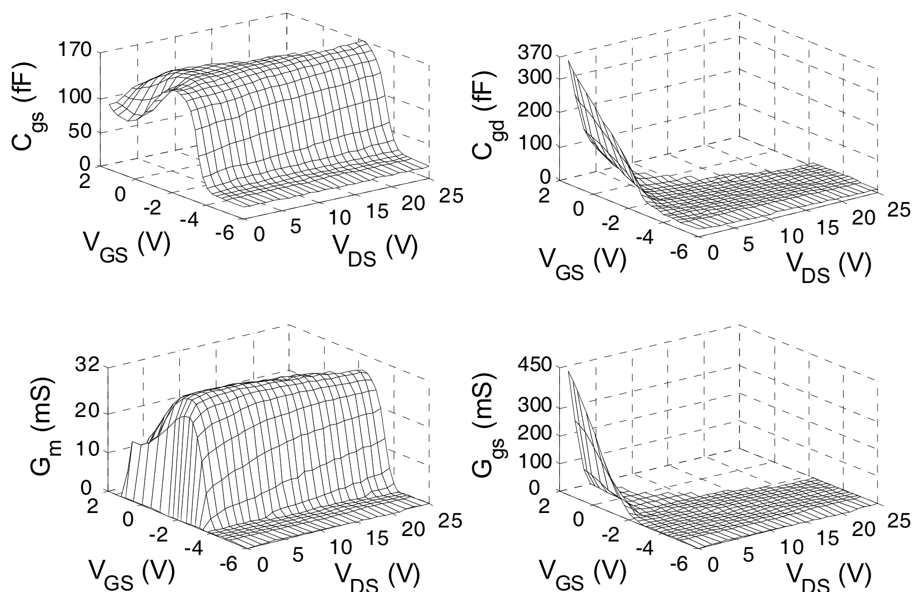

Fig. 7. Extracted C_{gs}, C_{gd}, G_m, and G_{ds} as a function of the extrinsic voltages for a GaN HEMT with a 2x50-μm gate width. © 2005 IEEE. Reprinted with permission.

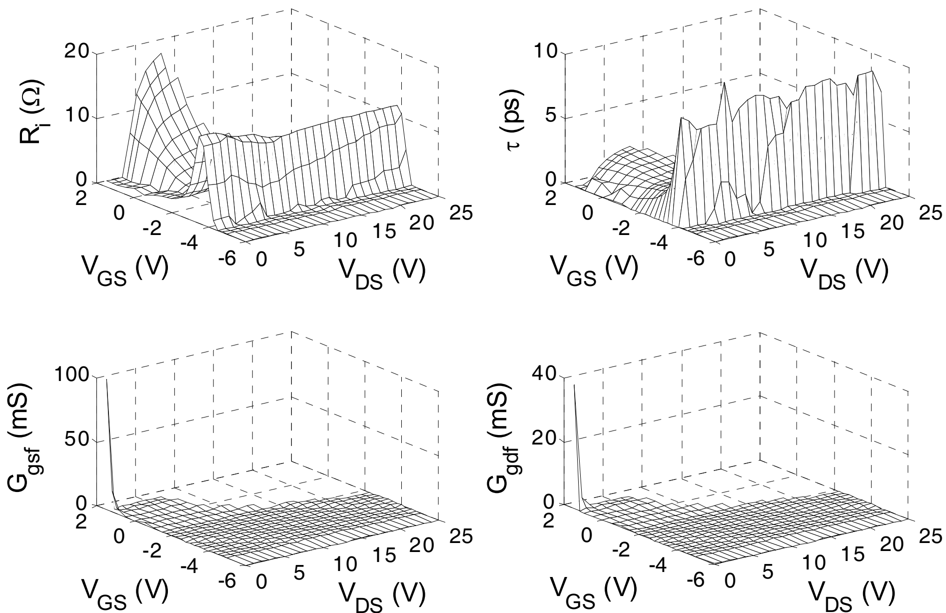

Fig. 8. Extracted R_i, τ, G_{gsf}, and G_{gdf} as a function of the extrinsic voltages for a GaN HEMT with a 2x50-μm gate width. © 2005 IEEE. Reprinted with permission.

τ can be determined from the plot of the phase of D versus ω by linear fitting. The admittance of the intrinsic drain–source branch Y_{ds} can be expressed as

$$Y_{ds} = Y_{i,22} + Y_{i,12} = G_{ds} + j\omega C_{ds} . \tag{41}$$

C_{ds} can be extracted from the plot of the imaginary part of Y_{ds} versus ω by linear fitting. Due to the frequency-dependent effect in the output conductance G_{ds}, its value is determined from the curve of $\omega\text{Re}[Y_{ds}]$ versus ω by linear fitting.

Figs. 6-8 present extracted intrinsic parameters for GaN HEMT using the proposed procedure under different extrinsic bias voltages. The extraction results show the typical expected characteristics of GaN HEMT. The reliability of the extraction results was demonstrated in (Jarndal & Kompa, 2005) in terms of the reverse modeling of the effective gate length for the same analysed devices. The accuracy of the proposed small signal modeling approach is verified through S-parameter simulation for different device sizes under different bias conditions. As it can be seen in Figs. 9 and 10, the model can simulate the S-parameter accurately. Also it can predict the kink effect in S_{22}, which occurs in larger size FETs (Lu et al., 2001).

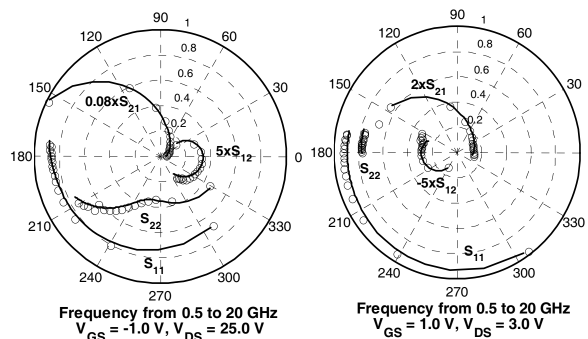

Fig. 9. Comparison of measured S-parameters of a 8x125-µm GaN HEMT (circles) with simulation results (lines) at (V_{GS} = -1, V_{DS} = 25 V) and (V_{GS} = 1 V, V_{DS} = 3 V). © 2006 IEEE. Reprinted with permission.

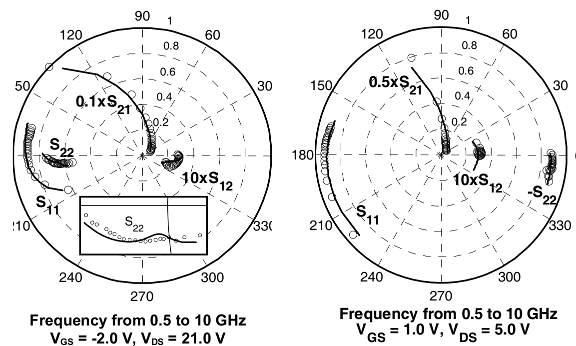

Fig. 10. Comparison of measured S-parameters of a 16x250-µm GaN HEMT (circles) with simulation results (lines) at (V_{GS} = -2, V_{DS} = 21 V) and (V_{GS} = 1 V, V_{DS} = 5 V). © 2006 IEEE. Reprinted with permission.

4. Large-signal modeling

Under RF large-signal operation, the values of the intrinsic-elements of the GaN HEMT model in Figure 2 vary with time and become dependent on the terminal voltages. Therefore the intrinsic part of this model can be described by the equivalent-circuit model shown in Figure 11. In this circuit, two quasi-static gate-current sources I_{gs} and I_{gd} and two quasi-static gate-charge sources Q_{gs} and Q_{gd} are used to describe the conduction and displacement currents. The nonquasi-static effect in the channel charge is approximately modeled with two bias-dependent resistors R_i and R_{gd} in series with Q_{gs} and Q_{gd}, respectively. This implementation is simpler and it improves the accuracy of the model up to millimeter-wave frequencies (Schmale & Kompa, 1997). A nonquasistatic drain-current model which accounts for trapping and self-heating effects is embedded in the proposed large-signal model. The drain-current value is determined by the applied intrinsic voltages V_{gs} and V_{ds}, whereas the amount of trapping induced current dispersion is controlled by the ac components of these voltages. These components are extracted from the intrinsic voltage

using RC high-pass circuits at gate and drain sides, as shown in Figure 11. The capacitors C_{GT} and C_{DT} values are selected to be 1 pF to provide a "macroscopic" modeling of charges stored in the surface and buffer traps. These charges are almost related to the leakage currents from the gate metal edge to the surface (Vetury et al., 2001) or from the channel into the buffer layer (Kohn et al., 2003). The small leakage currents in the gate and drain paths are realized with large (on the order of 1MΩ) resistances R_{GT} and R_{DT} in series with C_{GT} and C_{DT}, respectively.

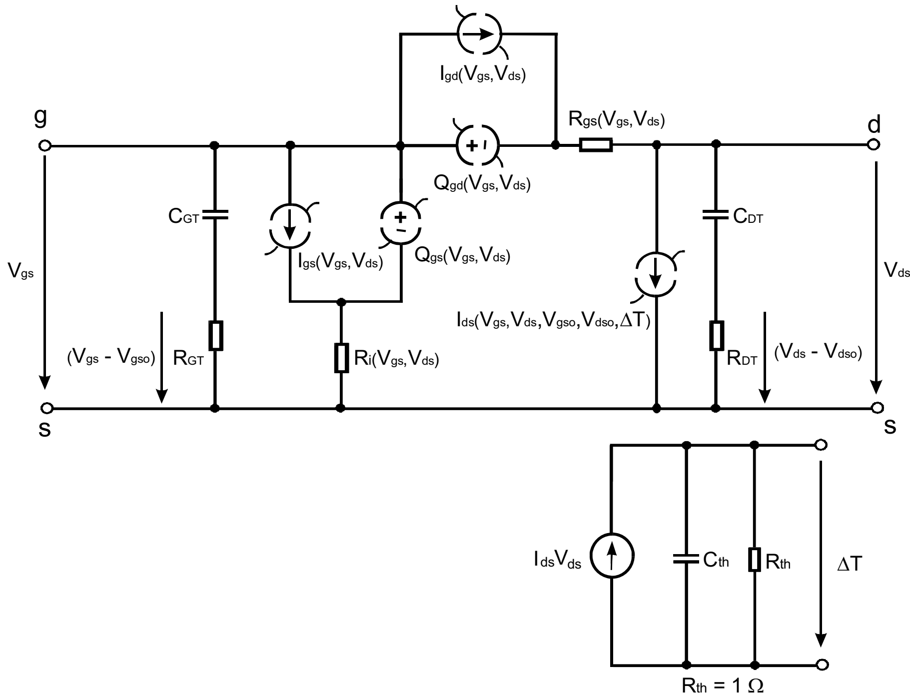

Fig. 11. Large-signal model for GaN HEMT including self-heating and trapping effects.

This implementation makes the equivalent circuit more physically meaningful; moreover, it improves the model accuracy for describing the low-frequency dispersion, as shown in Figure 12. This figure shows simulated frequency dispersion of the channel transconductance and output conductance, which is related mainly to the surface and buffer traps. The values of R_{GT}, R_{DT}, C_{GT}, and C_{DT} are chosen to result in trapping time constants on the order of $10^{-5} - 10^{-4}$ s (Meneghesso et al., 2001). In the current model, the amount of self-heating-induced current dispersion is controlled by normalized channel temperature rise ΔT. The normalized temperature rise is the channel temperature divided by the device thermal resistance R_{th}. A low-pass circuit is added to determine the value of ΔT due to the static and quasi-static dissipated power. The value of the thermal capacitance C_{th} is selected to define a transit time constant on the order of 1 ms (Kohn et al., 2003). R_{th} is normalized to one because its value is incorporated in thermal fitting parameter in the current-model expression, as will be discussed in section 4.2.

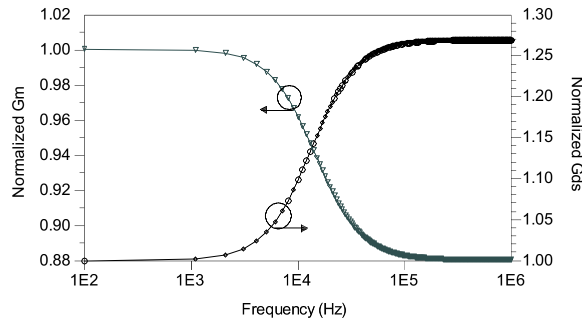

Fig. 12. Simulated normalized transconductance and output conductance for a 8x125-μm GaN HEMT at V_{DS} = 24 V and V_{GS} = -2 V.

4.1. Gate charge and current modeling

The intrinsic elements are extracted as a function of the extrinsic voltages V_{GS} and V_{DS} as presented in Figs. 6-8 for 2x50-μm GaN HEMT. To determine the intrinsic charge and current sources of the large-signal model by integration, a correction has to be carried out that considers the voltage drop across the extrinsic resistances. Therefore, the intrinsic voltages can be calculated as

$$V_{ds} = V_{DS} - (R_d + R_s) I_{ds} - R_s I_{gs} \tag{42}$$

$$V_{gs} = V_{GS} - (R_g + R_s) I_{gs} - R_s I_{ds} . \tag{43}$$

This implies that the values of the intrinsic voltages V_{gs} and V_{ds} are no longer equidistant, which makes the intrinsic-element integration difficult to achieve. In addition, this representation is not convenient to handle in Advanced Design System (ADS) simulator. Interpolation technique can be used to uniformly redistribute the intrinsic element data with respect to equidistant intrinsic voltages. However, the main limitations of this technique are that it produces discontinuities and an almost oscillating behavior in the interpolated data. These effects result in inaccurate simulation of higher order derivatives of the current and charge sources, which deteriorate output-power harmonics and IMD simulations (Cuoco et al., 2002). Therefore, B-spline-approximation technique is used for providing a uniform data for the intrinsic elements (Jarndal & Kompa, 2007). This technique can maintain the continuity of the data and its higher derivatives and hence improves the model simulation for the harmonics and the IMD (Koh et al., 2002). Generally, the intrinsic gate capacitances and conductances satisfy the integration path-independence rule (Root et al., 1991). Thus, the gate charges can be determined by integrating the intrinsic capacitances C_{gs}, C_{gd}, and C_{ds} as follows (Schmale & Kompa, 1997):

$$Q_{gs}(V_{gs}, V_{ds}) = \int_{V_{gs0}}^{V_{gs}} C_{gs}(V, V_{ds0})\, dV + \int_{V_{ds0}}^{V_{ds}} C_{ds}(V_{gs}, V)\, dV \tag{44}$$

Thank You for previewing this eBook

You can read the full version of this eBook in different formats:

- HTML (Free /Available to everyone)
- PDF / TXT (Available to V.I.P. members. Free Standard members can access up to 5 PDF/TXT eBooks per month each month)
- Epub & Mobipocket (Exclusive to V.I.P. members)

To download this full book, simply select the format you desire below